



# Design of quasicrystal alloys with favorable tribological performance in view of microstructure and mechanical properties

Kyungjun Lee<sup>a</sup>, Yan Chen<sup>b</sup>, Wei Dai<sup>a</sup>, Donald Naugle<sup>b,c</sup>, Hong Liang<sup>b,c,\*</sup>

<sup>a</sup> J. Mike Walker '66 Department of Mechanical Engineering, Texas A&M University, College Station, TX 77843-3123, United States

<sup>b</sup> Department of Physics & Astronomy, Texas A&M University, College Station, TX 77843, United States

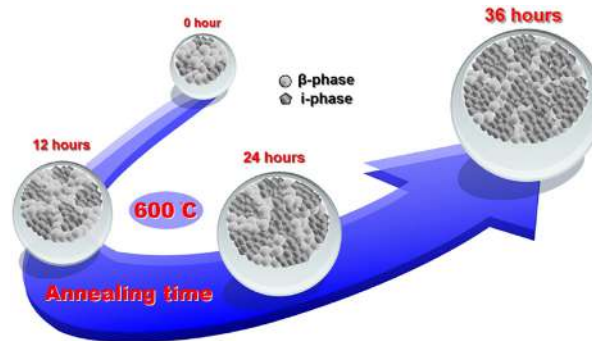
<sup>c</sup> Department of Materials Science and Engineering, Texas A&M University, College Station, TX 77843, United States

## HIGHLIGHTS

- Dual-phased quasicrystal alloys were developed by a simple processing procedure.
- The wear resistance is enhanced according to the increase of the i-phase.
- The ductile beta-phase in dual-phase quasicrystal alloys reduces the cracking.
- The optimal concentration of the two phases was found for the best tribological performance.

## GRAPHICAL ABSTRACT

Design of dual-phased quasicrystal alloys with different i-phase content; 59.24% (0 h), 68.85% (12h), 75.84% (24 h), and 81.75% (36 h) under a 600 °C annealing process. The higher content of i-phase in quasicrystal alloy shows a favorable tribological behavior because of the microstructure and mechanical properties of the dominant i-phase.



## ARTICLE INFO

### Article history:

Received 22 February 2020

Received in revised form 1 April 2020

Accepted 16 April 2020

Available online 05 May 2020

### Keywords:

Quasicrystal alloy

Microstructure, hardness

Impact test

Fracture toughness

Wear

## ABSTRACT

Quasicrystals have been used in various applications to improve wear resistance as well as friction. It is known that quasicrystal (i-phase) content and microstructure in alloys have a decisive effect on the mechanical properties and tribological performance. In this research, four ( $\beta + i$ )-dual-phased quasicrystal alloys with different i-phase content and grain size were developed to alleviate the brittleness of the i-phase with the help of the soft  $\beta$ -phase. The influences of the i-phase content and grain size were investigated through impact test, wear test, and analysis. Through the annealing process, the amount of the i-phase was increased by about 38% (59.24%  $\rightarrow$  81.75%), and, besides, the grain size of the i-phase was simultaneously increased from 3.47  $\mu\text{m}$  up to 9.98  $\mu\text{m}$ . As the amount of i-phase increased, it was possible to increase the hardness from 712 HV to 763 HV. Meanwhile, the increased grain size (i-phase) reduced the contact stress of the grain during wear testing; thus, the specific wear rate could be decreased from  $2.21 \times 10^{-4} \text{ mm}^3/\text{Nm}$  to  $0.5 \times 10^{-4} \text{ mm}^3/\text{Nm}$ . Not only that, but an experimental wear equation was obtained using empirical data to predict the wear behavior of the dual-phased alloys.

© 2020 Published by Elsevier Ltd. This is an open access article under the CC BY-NC-ND license (<http://creativecommons.org/licenses/by-nc-nd/4.0/>).

\* Corresponding author.

E-mail address: [hliang@tamu.edu](mailto:hliang@tamu.edu) (H. Liang).

Alloys and metal matrix composites (MMCs) are being developed for use as advanced materials. Because they are composed of two or more phases or materials, they show various and favorable mechanical and chemical properties depending on the combination of intrinsic compounds [1–7]. In this situation, quasicrystal alloys have emerged as a new material with enhanced material properties such as low thermal conductivity, high hardness, and low friction [8–12,14–16]. In addition, metallic phases of Al–Cu–Fe alloys are simply tailored by changing the concentration of raw materials [17,18]. The developed quasicrystal alloys have a microstructure composed of multi-phases like MMC and the microstructure's shape and size can be controlled through an annealing process. It has been reported that the change of the microstructures influences wear behavior and tribological performance [19–21]. Therefore, the microstructure effect on wear is actively studied by many researchers [22–32]. However, the use of the quasicrystal alloy has been limited due to its high brittleness [33–35]. In the present work, to alleviate the strong brittleness of the quasicrystal, the dual-phased quasicrystal alloy containing a ductile phase (beta-phase) was created with the arc-melting process. By adjusting the amount and shape of the quasicrystal phase (i-phase) by an annealing process, the wear mode and wear loss could be controlled. As a result, the presence of an optimal amount of the quasicrystal phase (i-phase) in the ductile phase (beta-phase) led to significant improvement in the tribological performance as well as the impact resistance. This is because the i-phase which has a strong resistance to plastic deformation reduced wear, and the beta-phase which is resistant to cracking decreased brittle fracture.

The mechanical properties and tribological performance of developed dual-phase alloys were investigated as a function of the change of shape and size distribution of the microstructure. Using statistical analysis, we identified critical factors that affect wear. This research enabled us to design alloys with favorable impact resistance and superior wear resistance. Additionally, the lifespan of the dual-phased alloy can be predicted through the experimental equation that we obtained.

## 2. Materials and experimental procedure

### 2.1. Materials and fabrication

Pure materials, aluminum (99.99 wt%, EM Science), copper (99.9 wt%, Chemisavers), and iron (99.98 wt%, Sigma-Aldrich) were used as raw metals to fabricate dual-phased quasicrystalline alloys. Quasicrystal alloys used in this research were selected from the ternary Al–Cu–Fe phase diagram. All alloys were developed by the arc-melting process and annealing process [17,18]. Finally, the selected ( $\beta + i$ ) dual-phase quasicrystal alloys had a stoichiometry of  $Al_{57}Cu_{33}Fe_{10}$ . Then, the samples were heated up to 600 °C to control the quantity and grain size of the i-phase.

### 2.2. Characterization of microstructure

After annealing, the as-cast alloys were mechanically polished with a polisher (STRUERS, DAP-3) and investigated chemically and mechanically. The chemical compositions of each phase were identified by X-ray diffraction (XRD, Rigacu) and energy-dispersive spectroscopy (EDS). Based on the results of XRD and EDS, the different colored regions on a scanning electron microscope (SEM, VEGA3-SB) backscattering image were matched to the phases identified by XRD. Then, the size and shape of each phase on polished surface morphology were examined. In order to calculate the volume fraction of each phase, Image J analysis was used for image processing and obtaining the area of each phase in Fig. S1. We extracted only i-phase area (gray area) from SEM image, and the area and the total number of the extracted each i-phase grain were obtained by the software. We assumed each of the

grains as a sphere, and the radius of each grain was obtained. Eventually, the volume fraction of the i-phase was calculated using the radius.

### 2.3. Indentation crack testing

In order to study the behavior of crack and fracture caused by impact force in terms of material removal, an indentation tester was designed with inspiration from ASTM D7136/D7136M, as shown in Fig. 1. By dropping a 200 g weight from 13 mm height with a 20  $\mu$ m tungsten carbide (WC) tip on the polished QC alloy's surface, a 2 N impulsive force occurred, and the impulsive force caused a 32,362 MPa contact stress between the WC tip and the contact surface. Heavier weights were not used because more than 200 g of weight could show the larger fracture area than the cross-section (max. 7 mm  $\times$  5 mm) of the sample we developed. Through the indentation test, 26 mJ energy was generated and transferred to the alloy surface. The impact energy eventually triggered cracking and fracture of the alloy. Indentation crack and fracture profiles of two selected samples (dual-phased and triple-phased QC alloys) were compared and evaluated with a scanning electron microscope and Image-J analysis.

### 2.4. Mechanical testing

A Vickers micro-indenter measured the hardness of four (4) different ( $\beta + i$ ) dual-phased alloys at a load of 100 gram-force (Tukon 1102). The fracture toughness of those samples was also obtained by the Vickers micro-indenter at a load of 200 gram-force by measuring crack length. Hardness and fracture toughness measurements were carried out seven times each to provide repeatability with standard deviations.

### 2.5. Wear testing

In order to find the correlation between hardness and fracture toughness on material failure, a designed tribological tester was used under the same set of conditions. A sufficiently slow sliding speed (3 mm/s) was applied in order to prevent tribochemical reactions as well as heating and oxidation during testing at room temperature. A 6 mm tungsten carbide (WC) ball was used in a dry reciprocating mode because of its super hardness and chemical stability. A tribometer (CSM Instrument) recorded a friction coefficient under 5 N normal load during total 1.5 m sliding movement. Each sample was tested three times. After the test, the samples were investigated by a scanning electron microscope (VGA3-SB) and an interferometer (ZYGO NewView 600) to reveal the wear mechanism.

## 3. Results and discussion

### 3.1. Dual-phased quasicrystal alloy

Multi-phased quasicrystal alloys with different chemical composition ratio ( $Al_{65}Cu_{20}Fe_{15}$  and  $Al_{57}Cu_{33}Fe_{10}$ ) were synthesized through two processes: arc-melting and annealing [17,18]. Phases of two alloys were identified using the X-ray diffraction pattern, as shown in Fig. 2 (a). The two multi-phased alloys were designated as ( $\lambda + \beta + i$ )-alloy and ( $\beta + i$ )-alloy. The ( $\lambda + \beta + i$ )-alloy showed excellent wear resistance compared to other multi-phased alloys thanks to a dominant i-phase (around 71%) [18]. However, the ( $\lambda + \beta + i$ )-alloy contained a lambda-phase of 17% as well. It was revealed that the lambda-phase was an extremely brittle material possessing high hardness and low fracture toughness in our previous paper [17]. Thus, the lambda-phase is quite vulnerable to impact and easily creates cracks and fractures. To compensate for this defect, a ( $\beta + i$ ) dual-phased quasicrystal alloy without the  $\lambda$ -phase was designed and developed. Based on the results of XRD and EDS, it was found that the light gray area of the ( $\beta + i$ )-alloy represented the  $\beta$ -phase and the gray area represented the i-phase in

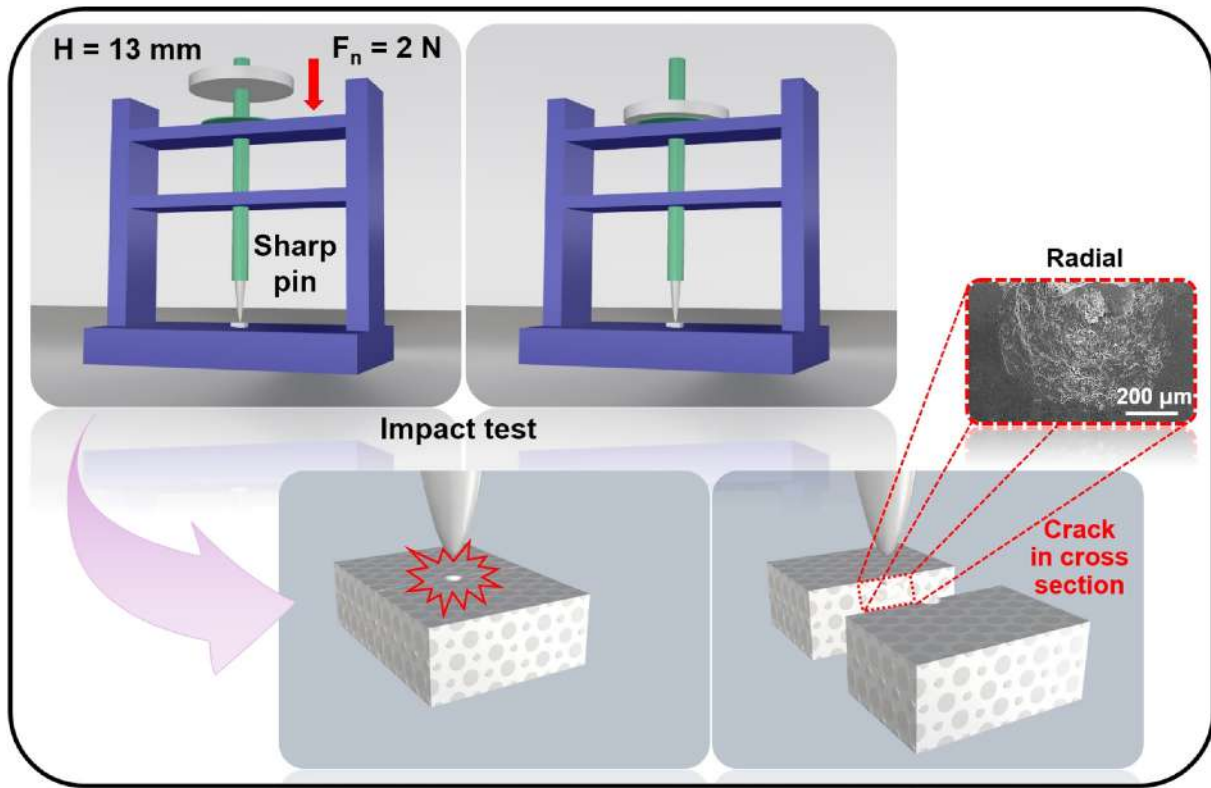


Fig. 1. Schematic of indentation test experimental setup.

Fig. 2(b). Although the  $(\beta + i)$ -alloy shows a relatively higher wear rate ( $2.2 \times 10^{-4} \text{ mm}^3/\text{Nm}$ ) than that of the  $(\lambda + \beta + i)$ -alloy ( $0.14 \times 10^{-4} \text{ mm}^3/\text{Nm}$ ) due to the lower content of the  $i$ -phase (around 60%), the  $(\beta + i)$ -alloy is expected to be favorable for impact as well as a brittle fracture. Because the  $(\beta + i)$ -alloy has relatively higher fracture toughness. In addition, the quantity of the  $i$ -phase in the  $(\beta + i)$ -alloy can be increased up to 81.75% by annealing for enhancing mechanical properties and tribological performance.

### 3.2. Crack and fracture

Two multi-phased quasicrystal alloys showed significantly different fracture behavior. Those behaviors were examined by the self-designed indentation tester. For the  $(\lambda + \beta + i)$ -alloy, the  $\lambda$ -phase accelerated crack propagation due to its little or no plastic deformation before failure. As a result, a broad fracture was observed in the  $(\lambda + \beta + i)$ -alloy which simultaneously showed combination geometries of a lateral and median crack in Fig. 3(a). In contrast, a smaller fracture of median crack was observed in the  $(\beta + i)$ -alloy since the  $\beta$ -phase reduced the possibility of crack and fracture by absorbing impact energy through plastic deformation.

After completing indentation crack tests, the fracture dimensions were gauged using SEM and image analysis. The results are summarized in Table 1. The  $(\beta + i)$ -alloy had a fracture of an average  $556.56 \mu\text{m} \pm 114.18 \mu\text{m}$  in width and an average  $411.13 \mu\text{m} \pm 85.32 \mu\text{m}$  in depth. For the  $(\lambda + \beta + i)$ -alloy, it showed two different crack modes: lateral crack mode and catastrophic crack mode, as shown in Fig. 3(b). The lateral crack in the  $(\lambda + \beta + i)$ -alloy exhibited smaller fracture area with an average  $616.69 \mu\text{m} \pm 95.65 \mu\text{m}$  width and an average  $274.63 \mu\text{m} \pm 135.17 \mu\text{m}$  depth, while the catastrophic crack in the  $(\lambda + \beta + i)$ -alloy generated approximately five times greater fracture than that of the lateral crack. The reason for two different crack modes can be found in the microstructures of the alloys. It means that these alloys do not have a perfect uniform microstructure. Accordingly, the crack

mode is reliant on the spot of indentation. Statistically, the probability of a catastrophic crack is 3 out of 8. The catastrophic crack leads to severe damage on the surface and the interior structure of the  $(\lambda + \beta + i)$ -alloy (damaged area by fracture:  $2.67 \times 10^6 \mu\text{m}^2 \pm 0.95 \times 10^6 \mu\text{m}^2$ ). This is because the  $\lambda$ -phase in the  $(\lambda + \beta + i)$ -alloy accelerates brittle fracture by supporting crack propagation in the extremely brittle material. To further understand the crack mode, the crack profiles of two alloys were examined at high magnification. The profile of the  $(\lambda + \beta + i)$ -alloy in Fig. 3(c) represents the lateral and median crack as the evidence of brittleness. In contrast, plastic deformation was prevalent in the  $(\beta + i)$ -alloy because the  $\beta$ -phase was soft. Based on these results, the  $\lambda$ -phase is considered as a main contributor to the catastrophic crack.

### 3.3. Controllable microstructure of dual-phased QC alloys

In this study, the  $(\beta + i)$ -alloy without the  $\lambda$ -phase was fabricated to enhance the alloy's mechanical properties and tribological performance. Our previously reported paper discovered the favorable wear resistance of the  $(\lambda + \beta + i)$ -alloy [17]. However, we also found that the  $\lambda$ -phase among the  $(\lambda + \beta + i)$ -phases makes the mechanical properties and tribological performance worse in terms of impact or wear. Therefore, the  $\lambda$ -phase was removed and dual phased  $(\beta + i)$ -alloy was developed to address this problem. The  $i$ -phase concentration of the  $(\beta + i)$ -alloy can be easily adjusted by using  $600^\circ\text{C}$  annealing as shown in Fig. 4(a). Basically, the unannealed  $(\beta + i)$ -alloy contains a 59.24% volume fraction of the  $i$ -phase. The volume fraction of  $i$ -phase rises proportionally with the annealing time: 68.85% (12 h), 75.84% (24 h), and 81.75% (36 h). Even the grain size of the  $i$ -phase also can be controlled from  $6.94 \mu\text{m}$  up to  $19.96 \mu\text{m}$  according to annealing time (0 h–36 h) in Fig. 4(b). From the grain size distribution of the  $i$ -phase, the unannealed  $(\beta + i)$ -alloy has 270 small-sized grains (Radius:  $3.47 \mu\text{m}$ ) per  $1.45 \times 10^5 \mu\text{m}^2$  area. The annealed  $(\beta + i)$ -alloy for

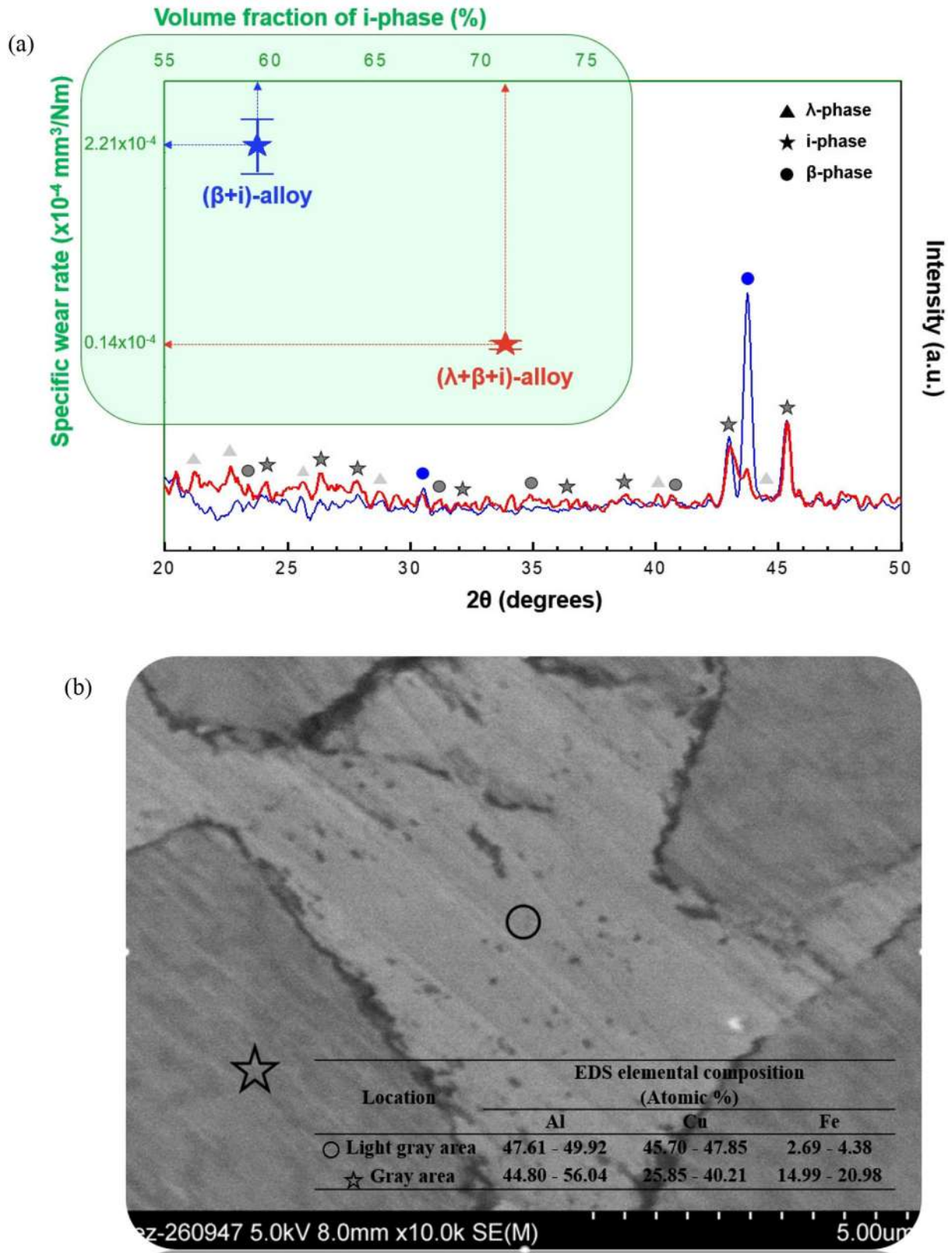
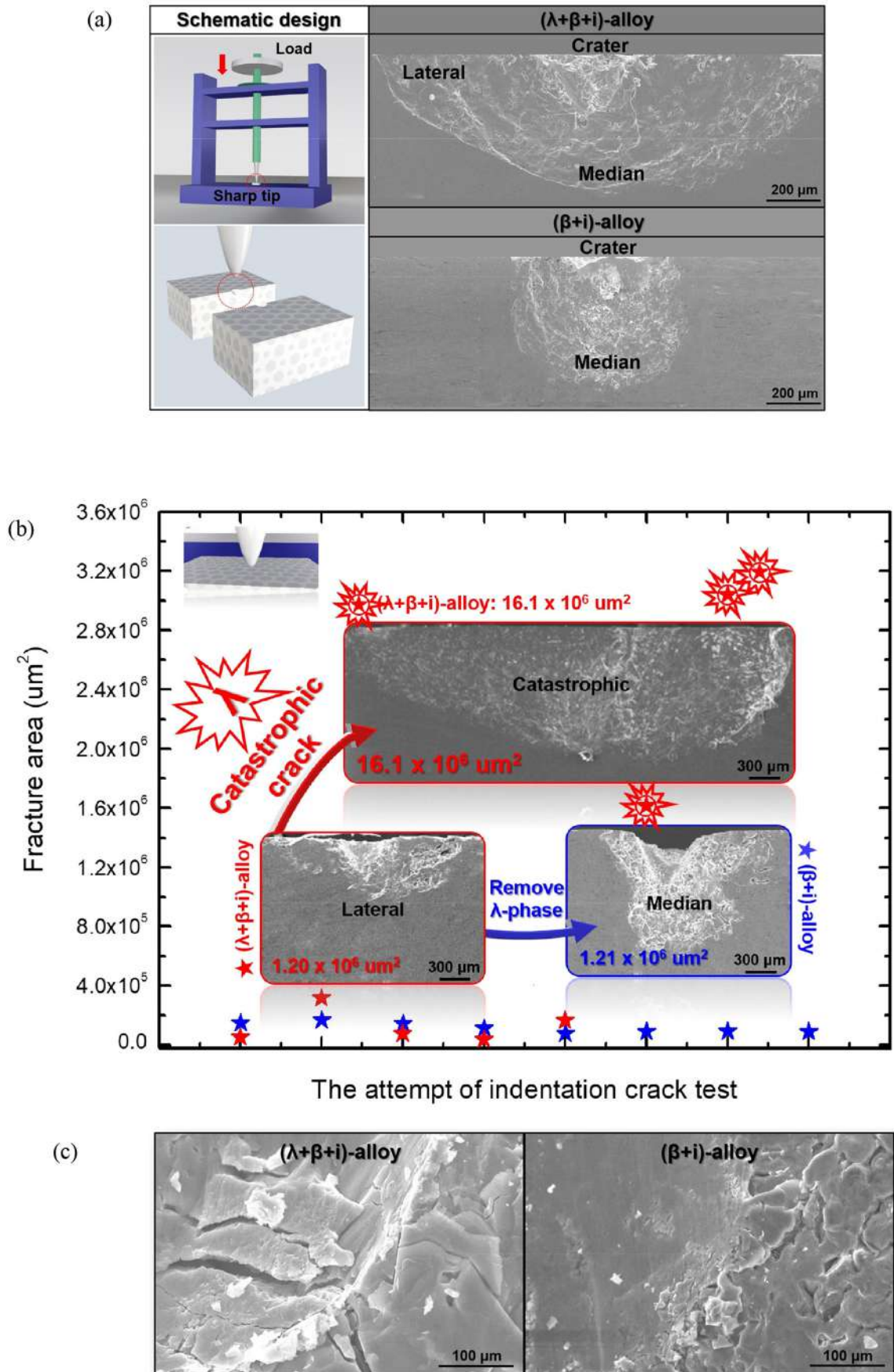


Fig. 2. (a) Comparison of the specific wear rate and the phase compositions between a ( $\lambda + \beta + i$ )-alloy and a ( $\beta + i$ )-alloy. (b) SEM image and EDS data of the ( $\beta + i$ )-alloy.

36 h has 23 large-sized grains (Radius: 9.98  $\mu$ m). Remaining two annealed ( $\beta + i$ )-alloys (12 h & 24 h) have a shrinking trend in the total number of grains and a rising tendency of grain size,

respectively (102 grains with 6.65  $\mu$ m radius & 35 grains with 8.62  $\mu$ m radius). These microstructure changes have a direct influence on mechanical properties and tribological behavior.



**Fig. 3.** Crack and fracture analysis by the indentation test of the  $(\lambda + \beta + i)$ -alloy and the  $(\beta + i)$ -alloy: (a) Two different types of crack geometries caused by the indentation testing, (b) comparison chart of the damaged area by fracture, and (c) crack profiles of two alloys.

**Table 1**  
Results of the indentation crack dimension test in the ( $\lambda + \beta + i$ )-alloy and the ( $\beta + i$ )-alloy.

Sample	Type	Indentation crack dimension								
		Width [ $\mu\text{m}$ ]			Depth [ $\mu\text{m}$ ]			Area [ $\mu\text{m}^2$ ]		
		Min.	Ave.	Max.	Min.	Ave.	Max.	Min.	Ave.	Max.
( $\lambda + \beta + i$ )-alloy	Lateral crack	516.75	616.69	741.09	149.49	274.63	464.75	36,841	65,749	164,099
	Catastrophic rupture	2587.41	3053.38	3519.75	893.75	1002.63	1111.5	1,614,155	2,671,692	3,439,228
( $\beta + i$ )-alloy	Median crack	412.75	556.56	708.51	315.25	411.13	539.52	83,905	121,067	172,445

### 3.4. Mechanical properties

#### 3.4.1. Hardness

The hardness of the ( $\beta + i$ )-alloys having different  $i$ -phase content was obtained utilizing a Vickers micro-indentation. The values are plotted in Fig. 5. The unannealed ( $\beta + i$ )-alloy containing an  $i$ -phase (59.24%) showed the lowest average hardness value 712 HV (34.58 standard deviations) that ranged from 652 HV to 741 HV. The hardness of the annealed 12 h ( $\beta + i$ )-alloy showed an average of 736 HV (49.69 standard deviations) between 645 HV to 753 HV. The ( $\beta + i$ )-alloy with 75.84% the  $i$ -phase showed a 750 HV (31.94 standard deviation) average value from 641 HV to 779 HV. In the case of the 36 hour-annealed ( $\beta + i$ )-alloy, the hardness reached up to 763 HV (37.18 standard deviations) with ranged 686 HV to 797 HV. The 81.75% volume fraction of the  $i$ -phase made the hardness of 36 hour-annealed alloy go up by 7.2% than that of an unannealed alloy (59.24%  $i$ -phase). Although the hardness is not substantially increased, it is expected to influence significantly wear behavior due to the changes in the microstructure and toughness of the alloy. As another advantage of this experiment, the hardness of the ( $\beta + i$ )-alloy is predictable using an experimental hardness equation obtained based on the results:  $Y = -1.034 \times 10^{-2} X^2 + 3.821 X + 521.589$  (where,  $Y$  represents the Vickers hardness and  $X$  represents the concentration of the  $i$ -phase).

#### 3.4.2. Fracture toughness

In the previous research, we reported that although increased fracture toughness would decrease the overall hardness of the alloy, it would enhance wear resistance at the same time by reducing brittle fracture [17]. Thus, the optimal concentration of the  $i$ -phase should be determined in order to develop the alloy with the best tribological performance. As a first step, the fracture toughness of the ( $\beta + i$ )-alloys was measured with a Vickers micro-indentation. The measured values were plotted in Fig. 6. The unannealed ( $\beta + i$ )-alloy had the highest fracture toughness  $1.878 \text{ MPa} \cdot \text{m}^{0.5}$  (0.246 standard deviations) with an average value ranging from  $1.572 \text{ MPa} \cdot \text{m}^{0.5}$  to  $2.149 \text{ MPa} \cdot \text{m}^{0.5}$ . Contrary to the unannealed alloy, the ( $\beta + i$ )-alloys annealed for 36 h had the lowest fracture toughness  $1.718 \text{ MPa} \cdot \text{m}^{0.5}$  (0.238 standard deviations) with an average value ranging from  $1.477 \text{ MPa} \cdot \text{m}^{0.5}$  to  $1.990 \text{ MPa} \cdot \text{m}^{0.5}$ . The alloy annealed for 12 h and that annealed for 24 h had fracture toughness  $1.813 \text{ MPa} \cdot \text{m}^{0.5}$  ( $1.673$ – $1.987 \text{ MPa} \cdot \text{m}^{0.5}$  range with 0.163 standard deviations) and fracture toughness  $1.771 \text{ MPa} \cdot \text{m}^{0.5}$  ( $1.618$ – $2.063 \text{ MPa} \cdot \text{m}^{0.5}$  range with 0.182 standard deviations), respectively. The plotted curve of the fracture toughness tends to decrease with an increase in  $i$ -phase concentration. That means they are inversely related to each other. Because increased  $i$ -phase reduces the ductility of the alloys. The inserted chart (violet dotted line) in Fig. 6 clearly shows that there is a strong inverse proportion between  $\beta$ -phase concentration (fracture toughness) and  $i$ -phase concentration (hardness). The fracture toughness can be predicted using the fitted equation (blue dotted line):  $Y = -3.128 \times 10^{-6} X^2 - 5.490 X + 2.203$  (where,  $Y$  represents the fracture toughness and  $X$  represents the concentration of the  $i$ -phase).

### 3.5. Tribological performance

#### 3.5.1. Effect of $i$ -phase concentration

Wear scars of four ( $\beta + i$ )-alloys (Annealing time 0 h–36 h) were examined with a scanning electron microscope and an interferometer. The specific wear rate of each sample was obtained by dividing a wear volume by the load and total sliding distance. In Fig. 7(a), wear scars of the unannealed sample showed grooves and plows with a depth ( $2.32 \mu\text{m}$ ) and a width ( $225 \mu\text{m}$ ) along the sliding direction, indicating abrasive wear. The samples with increased annealing time exhibit shallower wear grooves. Even grooves and plows were rare in the sample annealed for 36 h which had a wear track depth of  $0.86 \mu\text{m}$  and a width of  $180 \mu\text{m}$ . Because the sample has enough high resistance to localized plastic deformation. In contrast, the surfaces of both unannealed sample and the sample annealed for 12 h showed delaminated areas, which was identified as adhesive wear. That's because all ( $\beta + i$ )-alloys contained different sizes of  $i$ -phase grain ( $3.47 \mu\text{m}$  radius to  $9.98 \mu\text{m}$  radius). When the ( $\beta + i$ )-alloy had the smaller  $i$ -phase grains, spallation easily occurred due to reduced contact area with the beta-phase matrix. As a result, the combination of two factors ( $i$ -phase concentration and  $i$ -phase grain size) determined the wear resistance. The ranking of wear resistance is the unannealed alloy ( $2.21 \times 10^{-4} \text{ mm}^3/\text{Nm} \pm 0.20 \times 10^{-4} \text{ mm}^3/\text{Nm}$ ) < the 12 hour-annealed alloy ( $1.16 \times 10^{-4} \text{ mm}^3/\text{Nm} \pm 0.41 \times 10^{-4} \text{ mm}^3/\text{Nm}$ ) < the 24 hour-annealed alloy ( $1.05 \times 10^{-4} \text{ mm}^3/\text{Nm} \pm 0.56 \times 10^{-5} \text{ mm}^3/\text{Nm}$ ) < the 36 h-annealed alloy ( $0.50 \times 10^{-4} \text{ mm}^3/\text{Nm} \pm 0.20 \times 10^{-5} \text{ mm}^3/\text{Nm}$ ).

We are also able to approach wear analysis from the viewpoint of the mechanical properties. The mechanical properties of the ( $\beta + i$ )-alloys are found to depend on the  $i$ -phase concentration and the grain size. Eventually, the specific wear rates are determined by the values of the hardness and the fracture toughness as results in our previous papers [17,18]. The hardness, fraction toughness, and specific wear rate of the ( $\beta + i$ )-alloys are plotted in Fig. 7(b). While the hardness (red-dotted line) rises, the fracture toughness decreases along with the quadratic equations obtained by the experiment (blue-dotted line). Therefore, the optimal concentration of the  $i$ -phase, which shows the lowest specific wear rate, can be determined as the  $x$ -axis value of the vertex of the specific wear rate trend curve plotted by experimental values (green-dotted line):  $Y = 2.124 \times 10^{-7} X^2 - 3.3669 \times 10^{-5} X + 1.640 \times 10^{-3}$  ( $Y$  represents the specific wear rate and  $X$  represents the concentration of the  $i$ -phase). The experimental quadratic equation of the specific wear rate shows a minimum wear rate ( $0.55 \times 10^{-4} \text{ mm}^3/\text{Nm}$ ) when the concentration of the  $i$ -phase is 86.37 wt%. In order words, the two properties (Hardness and Fracture toughness) that are in inverse relationship indicate that they are best tribologically combined at the optimum concentration (86.37 wt%) of the  $i$ -phase. If the concentration of the  $i$ -phase in the ( $\beta + i$ )-alloy is less than 86.37 wt%, material removal is dominant and increased due to lack of hardness. On the contrary, material failure begins to increase by brittle fracture beyond that concentration (86.37 wt%) since the  $\beta$ -phase (soft material) barely exists in the ( $\beta + i$ )-alloy.

#### 3.5.2. Effects of $i$ -phase's grain size

Generally, the degree of wear has a negative relationship with hardness according to Archard's equation. Actual wear mode is rarely that

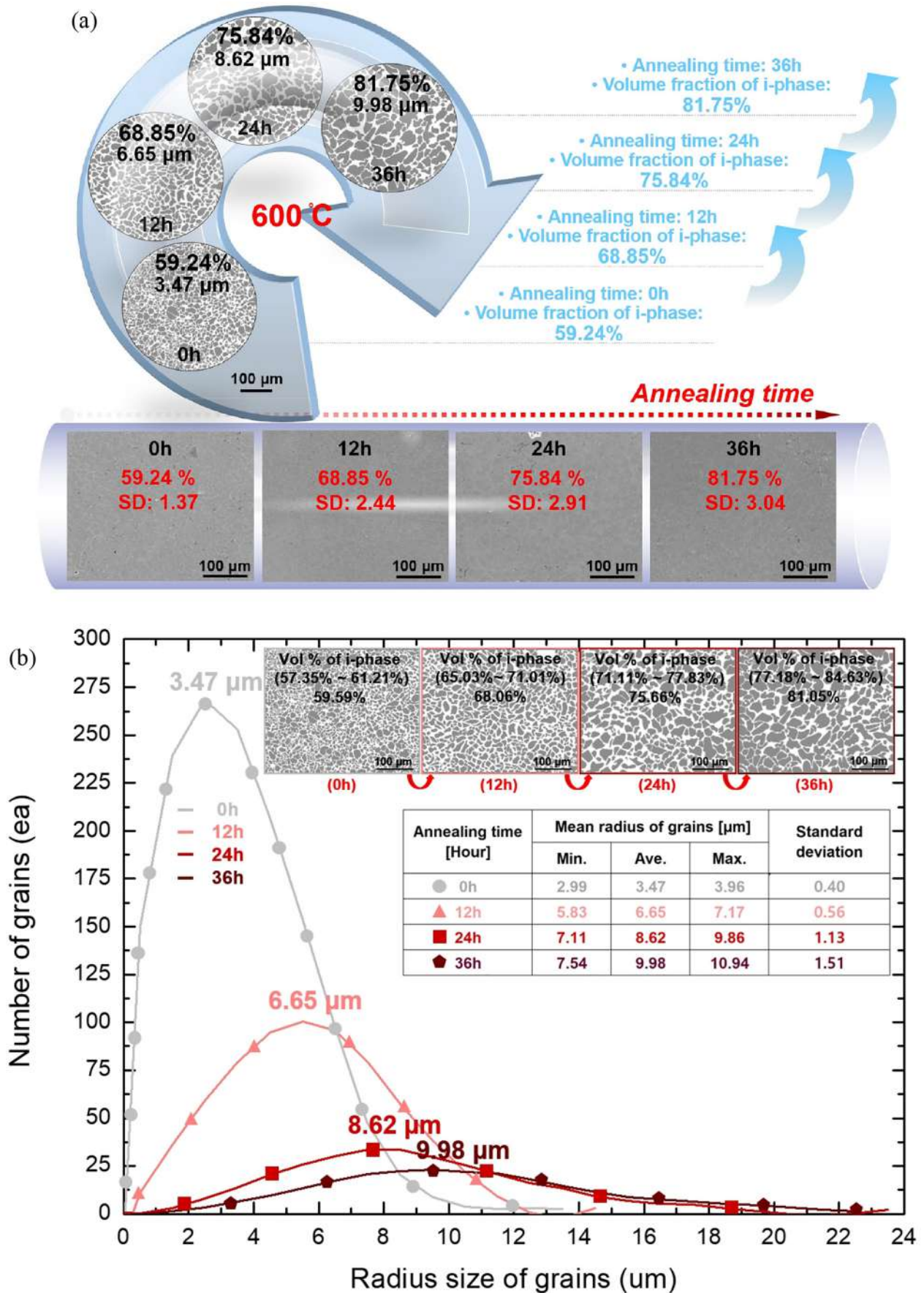


Fig. 4. (a) Controlling process of the content and grain size of the i-phase in the (β + i)-alloy according to annealing time and (b) grain size distribution of the i-phase according to annealing time.

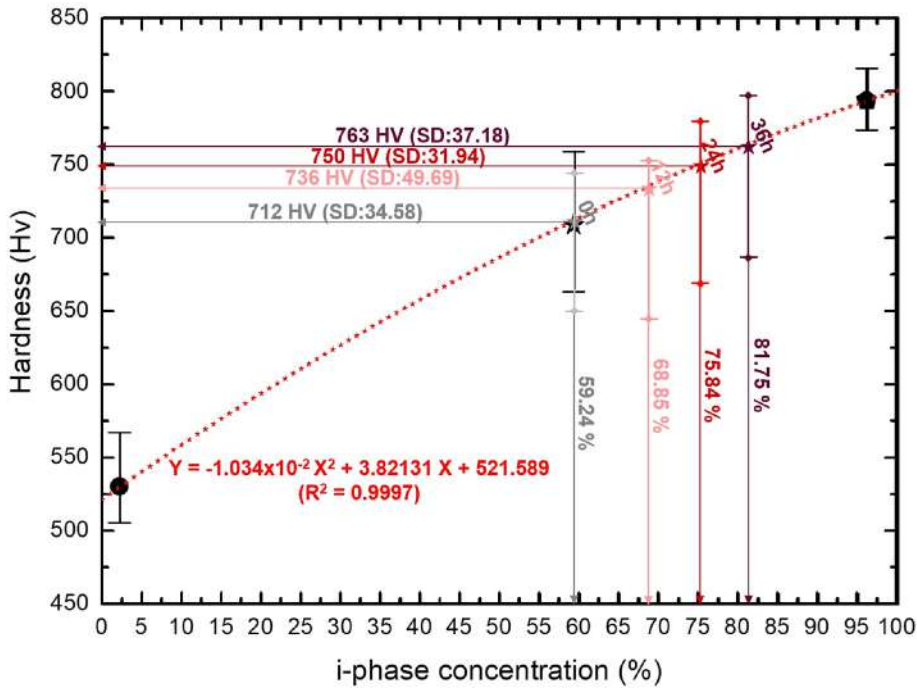


Fig. 5. Experimentally obtained hardness values and the curve fit (red dotted line) as a function of i-phase concentration. (For interpretation of the references to color in this figure legend, the reader is referred to the web version of this article.)

simple in the case of alloys with multiple phases or composites with reinforcement. Thus, to understand the wear mechanism of the ( $\beta + i$ )-alloy, the effect of the microstructure should be considered. Our results show a similar tendency: the higher the i-phase concentration in the sample, the better wear resistance the sample shows. However, the relationship between the mechanical property and tribological performance is not linear. The reason is that the tribological performance varies depending on the contact stress caused according to the grain size (i-phase), and the frequency of cracking by the generated contact

stress. Even materials with extremely high hardness can be more abrasive due to brittle fracture [36]. The dual-phased quasicrystal alloy consists of the  $\beta$ -phase and i-phase. Grains of the i-phase are located in the beta-phase matrix as a reinforcement like a concept of composites. The grain size analysis was already described in Section 3.3 Controllable Microstructure of Dual-Phased QC alloys. The contact stress of the i-phase grain was calculated under a 5 N load with the aid of the Abaqus simulation in Fig. 8. The smallest single grain (Radius 3.47  $\mu\text{m}$ ) of the i-phase (without annealing) generated the highest contact stress of 24.89 GPa

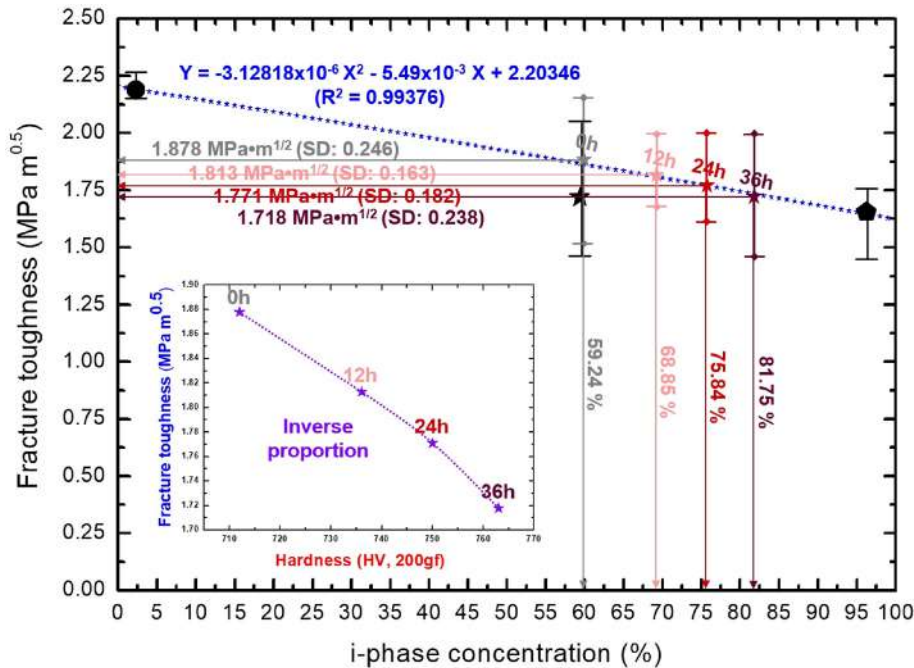


Fig. 6. Experimentally obtained fracture toughness values and the fitted curve (blue dotted line) as a function of the i-phase concentration. (For interpretation of the references to color in this figure legend, the reader is referred to the web version of this article.)

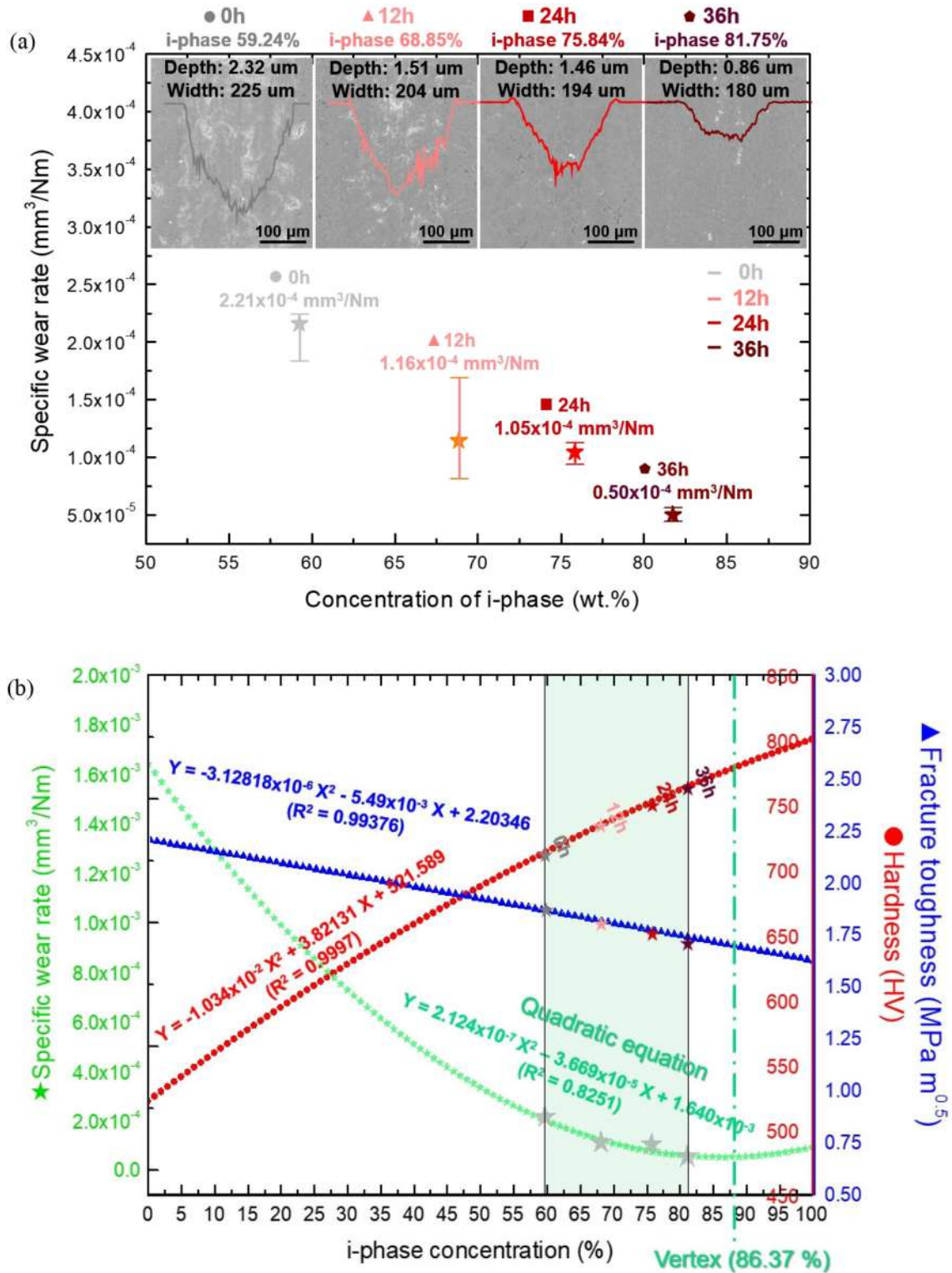


Fig. 7. Specific wear rates as a function of the concentration of the i-phase. (a) microstructure and measured profiles of worn surfaces for four (β + i)-alloys and (b) hardness and fracture toughness plots of four (β + i)-alloys and the quadratic equation fit.

because it had the smallest contact area under the same pressure. On the other hand, decreased contact stress is attributed to the growth of the contact area as the grains increase. Accordingly, grains (Radius: 9.98 μm) in the (β + i)-alloy annealed for 36 h generate the smallest contact stress value (22.21 GPa). The higher contact stress forces a grain to protrude and escape from the surface during wear testing like

insert SEM images (0 h and 12 h annealed samples) in Fig. 8(a). The missing grains accelerated a material loss. For this reason, the large number of cracks observed in the grain boundary between beta-phase and i-phase (0 h and 12 h annealed samples, Fig. 8(b)) worsen the wear resistance. Therefore, in the case of 24 h and 36 h annealed samples, they show more favorable wear resistance thanks to the lower

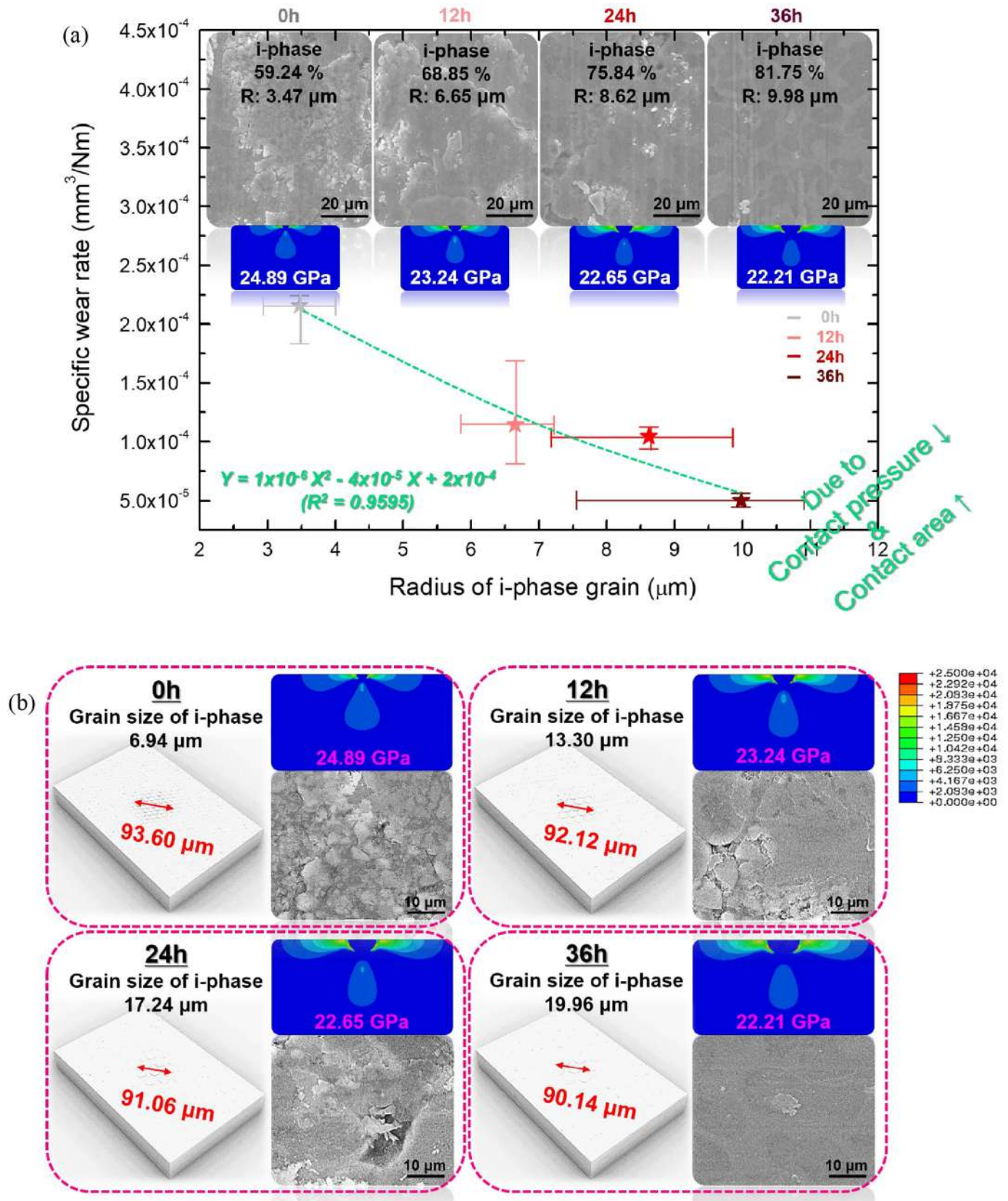


Fig. 8. (a) Relationship between the grain size of the i-phase and the specific wear rate. (b) Contact stress simulation and degree of wear of each ( $\beta + i$ )-alloy (0 h–36 h annealing).

contact stress (22.65 GPa and 22.21 GPa) as well as fewer grain boundaries. As a result, cracks and missing grains in the ( $\beta + i$ )-alloy annealed for 36 h among the four samples were almost out of observable.

We found that the high fracture toughness enhances the wear resistance by preventing crack and fracture in our previous research [17,18]. In this research, contrary to expectations, our results about the specific

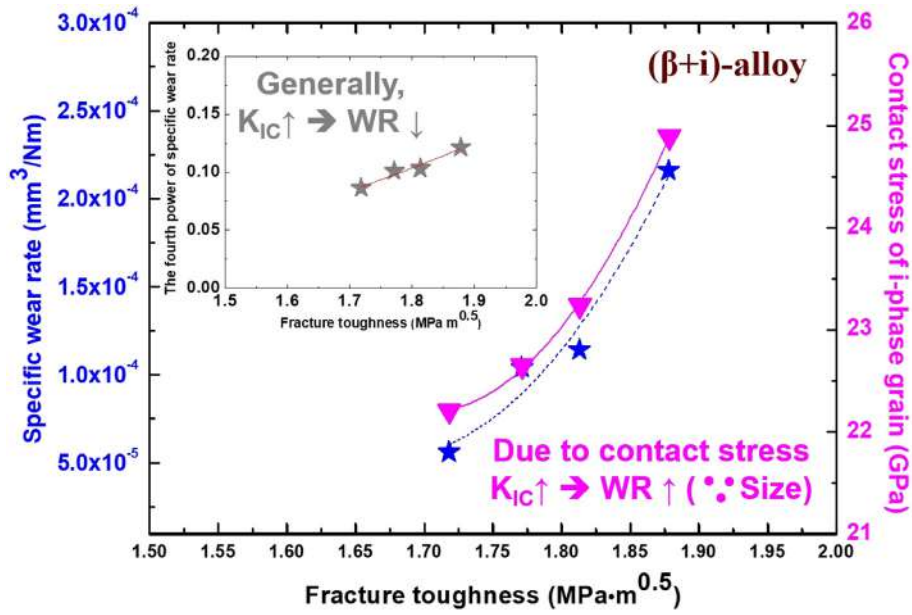


Fig. 9. Specific wear rate and contact pressure of i-phase grain plotted as a function of fracture toughness in four (β + i)-alloys.

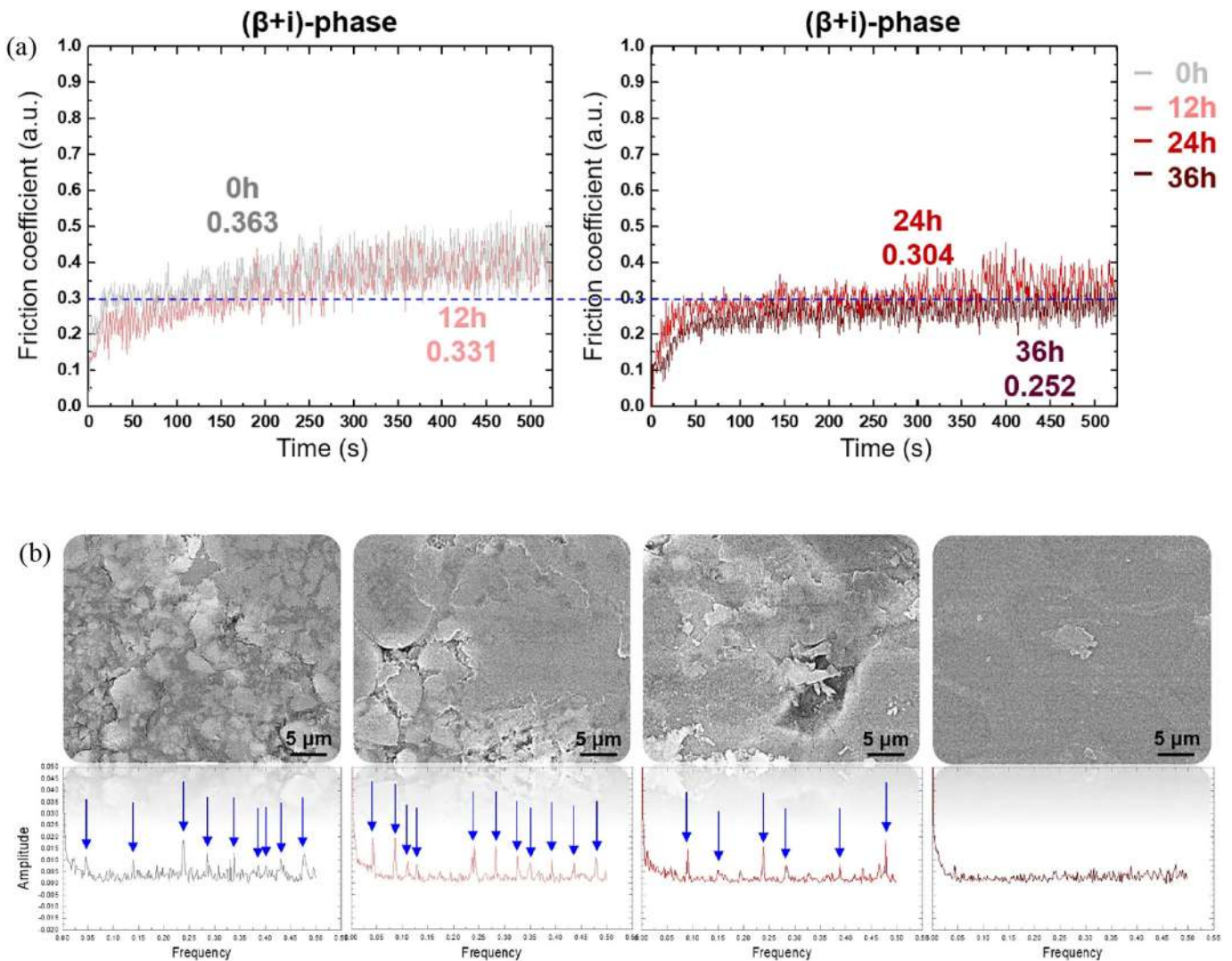


Fig. 10. (a) Variation of friction coefficient according to annealing time in four samples. (b) Indirect evaluation of crack or wear using fast Fourier transform.

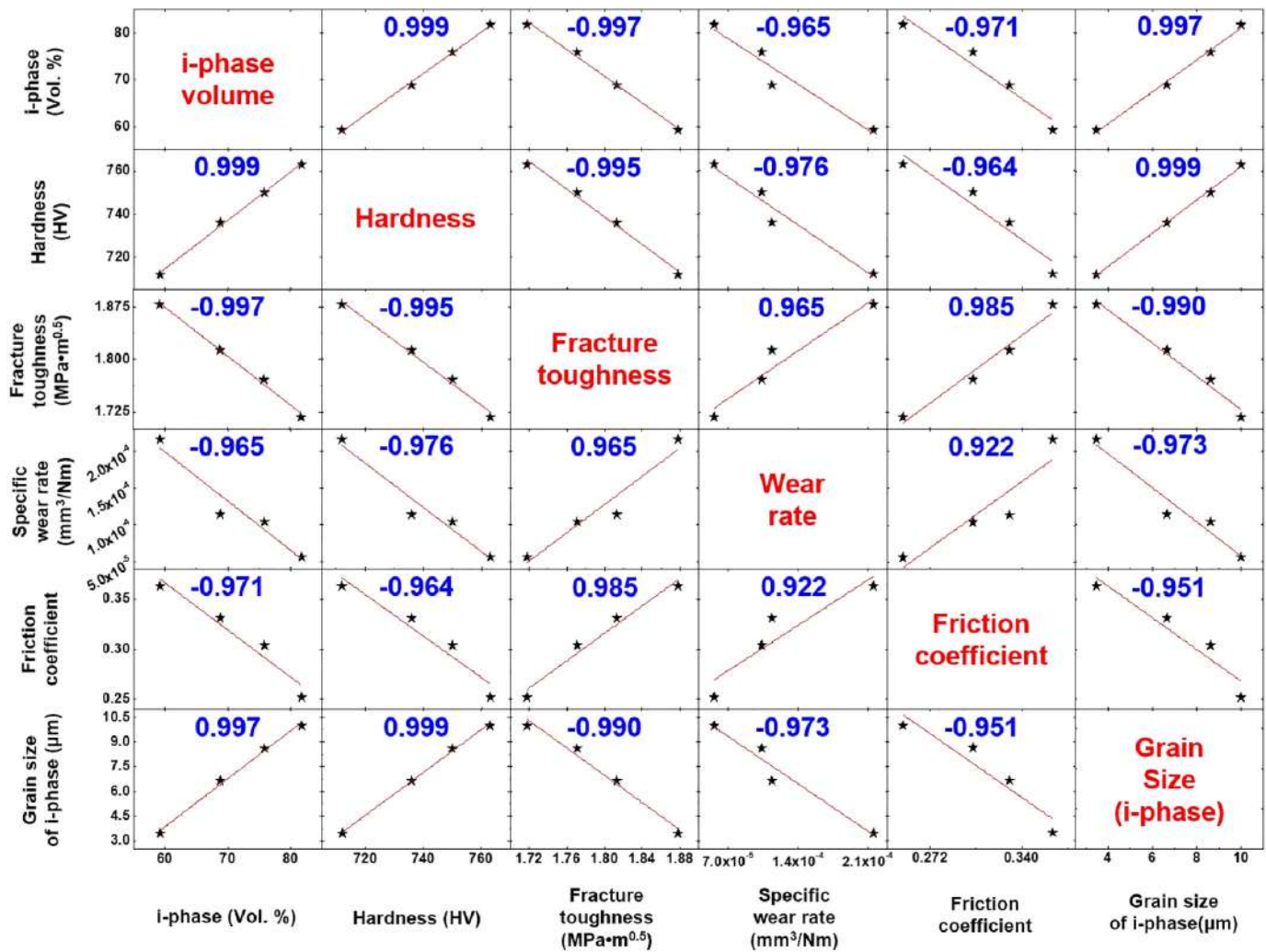


Fig. 11. Scatterplot matrix of the volume of i-phase and mechanical & tribological factors.

wear rate were totally different. We found that the softer it is, the greater the wear, as shown in Fig. 9. The reason is associated with the contact stress. Because the contact stress of the i-phase grain has increased with the increase of the fracture toughness, the increased contact stress makes the bonding between the interface of two phases break and the grains easily come out from the ( $\beta + i$ )-dual phased material. As a result, increased fracture toughness leads to more wear. Thus, microstructure must be considered with the mechanical properties for the comprehensive understanding of the wear mechanism.

### 3.6. Frictional performance

The friction coefficient of the four samples (annealing time: 0 h–36 h) against a 6 mm WC ball was recorded during wear testing, as shown in Fig. 10(a). While the unannealed sample is composed of the i-phase (59.24 wt%) which shows the highest friction coefficient value (0.363), the sample annealed for 36 h shows the lowest friction coefficient value (0.252) because the sample contains 81.75% i-phase. The remaining samples (12 hour-annealed and 24 hour-annealed samples) show friction coefficients of 0.331 and 0.304, respectively. From this result, we can conclude that there is a negative correlation between the annealing time and the friction coefficient. That is, longer annealing duration leads to an increase in the volume fraction of the i-phase. Increased i-phase plays an important role in terms of friction reduction. Therefore, the use of the alloy with high i-phase concentration is able

to save kinetic energy or thermal energy when surfaces in contact move relative to each other.

The degree of crack or wear was again evaluated using the indirect method (Fast Fourier Transform). The recorded data of the friction coefficient was transformed to amplitude and frequency chart in Fig. 10(b). The friction coefficient shows high peaks on the spots having a crack or material removal. Numerous strong peaks were periodically observed in the FFT chart of two alloys (0 h and 12 h). However, the periodic strong peaks were moderated as the annealing time increased. Finally, the peaks were not observed in the alloy (36 h) because crack and material removal did not exist during wear testing. We can easily identify the existence or nonexistence of material failure with only friction data.

### 3.7. Correlation between i-phase and other factors

The ( $\beta + i$ )-dual phased alloys were investigated in various ways. Among them, six types of factors were selected for correlation analysis: volume of i-phase, hardness, fracture toughness, wear rate, friction coefficient, and grain size of i-phase. According to the statistical correlation chart in Fig. 11, the volume of the i-phase showed a high correlation with others overall. Especially, it has a strong positive correlation with hardness (0.999). Meanwhile, fracture toughness ( $-0.997$ ) shows a strong negative correlation with the volume of the i-phase. Statistical results allow us to confirm their inverse relationship again. The hardness ( $-0.976$ ) of the alloy plays the most important role in determining the degree of wear rate. Next, the grain size of the i-phase ( $-0.973$ ) is

also a dominant contributor on wear. Consequently, microstructure inevitably has to be studied for the wear mechanism.

#### 4. Conclusions

Among a series of quasicrystal alloys containing different phases, the ( $\beta + i$ )-dual phased alloy ( $Al_{57}Cu_{33}Fe_{10}$ ) was chosen and then prepared by a two-step process (arc-melting and annealing). The dual-phase alloy is composed of beta and icosahedral phases. The beta-phase increases the ductility of the alloy as a matrix by completely covering the round shape of the i-phase like so many reinforced composites. Therefore, the ( $\beta + i$ )-alloys possess both high hardness and favorable fracture toughness, which leads to improved wear resistance as well as impact resistance. The annealing process is able to adjust the concentration (from 59.25 wt% to 81.75 wt%) and the grain size of the i-phase (from 3.47  $\mu m$  to 9.98  $\mu m$ ). Based on all experimental results, the wear resistance of the quasicrystal alloy with the highest concentration of the i-phase was improved around 77.38% compared to that of the quasicrystal alloy with the lowest concentration due to the higher hardness and the lower contact stress. In addition, the friction coefficient was also improved by up to 30.58%.

Additionally, the experimental equations were obtained. They will be useful to determine the optimal conditions and predict the life span of the material. Interesting results revealed in this research can lead to future studies that focus on the corrosion behavior of quasicrystal alloys.

#### CRedit authorship contribution statement

**Kyungjun Lee:** Investigation, Writing - original draft. **Yan Chen:** Investigation, Formal analysis, Writing - review & editing. **Wei Dai:** Investigation, Formal analysis, Writing - review & editing. **Donald Naugle:** Methodology, Writing - review & editing. **Hong Liang:** Conceptualization, Formal analysis, Writing - original draft.

#### Declaration of competing interest

Authors declare that there is no conflict of interests.

#### Acknowledgments

The authors would like to thank the assistance of Dr. Daya Rathnayaka during the manufacturing of alloys. DGN acknowledges the support of the Robert A. Welch Foundation, Houston, TX (Grant No. A-0514). Part of this work was supported by the Turbomachinery Research Laboratory at Texas A&M University.

#### Appendix A. Supplementary data

Supplementary data to this article can be found online at <https://doi.org/10.1016/j.matdes.2020.108735>.

#### References

- [1] B. Mallik, K. Sikdar, D. Roy, Tribological performance of in situ reinforced Al-based metal matrix composite processed by plasma sintering, *Mater. Perform. Charact.* 8 (2019) 20180123–20190171, <https://doi.org/10.1520/MPC20180123>.
- [2] G. Lu, X. Shi, X. Liu, H. Zhou, Y. Chen, Z. Yang, Y. Huang, Tribological performance of functionally gradient structure of graphene nanoplatelets reinforced  $Ni_3Al$  metal matrix composites prepared by laser melting deposition, *Wear* 428–429 (2019) 417–429, <https://doi.org/10.1016/j.wear.2019.04.009>.
- [3] E. Salur, A. Aslan, M. Kuntoglu, A. Gunes, O.S. Sahin, Experimental study and analysis of machinability characteristics of metal matrix composites during drilling, *Compos. Part B* 166 (2019) 401–413, <https://doi.org/10.1016/j.compositesb.2019.02.023>.
- [4] W. Bai, A. Roy, R. Sun, V.V. Silberschmidt, Enhanced machinability of SiC-reinforced metal-matrix composite with hybrid turning, *J. Mater. Process. Technol.* 268 (2019) 149–161, <https://doi.org/10.1016/j.jmatprotec.2019.01.017>.
- [5] M. Ozerov, M. Klimova, V. Sokolovskiy, N. Stepanov, A. Popov, M. Boldin, S. Zherebtsov, Evolution of microstructure and mechanical properties of Ti/TiB metal-matrix composite during isothermal multiaxial forging, *J. Alloys Compd.* 770 (2019) 840–848, <https://doi.org/10.1016/j.jallcom.2018.08.215>.
- [6] S. Marimuthu, J. Dunleavy, Y. Liu, M. Antar, B. Smith, Laser cutting of aluminium-alumina metal matrix composite, *Opt. Laser Technol.* 117 (2019) 251–259, <https://doi.org/10.1016/j.optlastec.2019.04.029>.
- [7] N.T. Hegde, D. Pai, R. Hegde, Heat treatment and mechanical characterization of LM-25/tungsten carbide metal matrix composites, *Mater. Today: Proc.* 8 (2019) 810–817, <https://doi.org/10.1016/j.matpr.2019.08.136>.
- [8] M.F. Ozaydin, H. Liang, Design and synthesis of a geopolymer-enhanced quasicrystalline composite for resisting wear and corrosion, *J. Tribol.* 138 (2) (2015), 021601. <https://doi.org/10.1115/1.4031400>.
- [9] B.E. Puckermann, *Quasicrystals: Types, Systems, and Techniques*, Nova Science Publishers, United States, 2010 [http://www.novapublishers.org/catalog/product\\_info.php?products\\_id=12894](http://www.novapublishers.org/catalog/product_info.php?products_id=12894).
- [10] J.-M. Dubois, *Useful Quasicrystals*, World Scientific, 2005 <https://doi.org/10.1142/3585>.
- [11] H. Parsamehr, C.-L. Yang, W.-T. Liu, S.-W. Chen, S.-Y. Chang, L.-J. Chen, A.P. Tsai, C.-H. Lai, Direct observation of growth and stability of Al-Cu-Fe quasicrystal thin films, *Acta Mater.* 174 (2019) 1–8, <https://doi.org/10.1016/j.actamat.2019.05.024>.
- [12] X. Lan, H. Wang, Z. Sun, X. Jiang, Al-Cu-Fe quasicrystals as the anode for lithium ion batteries, *J. Alloys Compd.* 805 (2019) 942–946, <https://doi.org/10.1016/j.jallcom.2019.07.148>.
- [13] Z. Li, S. Pan, S. Zhang, S. Feng, M. Li, R. Liu, Y. Tian, L.-m. Wang, Preparation of bulk metallic glasses by modifying local structure of icosahedral quasicrystals, *Intermetallics* 109 (2019) 97–104, <https://doi.org/10.1016/j.intermet.2019.03.007>.
- [14] X. Xi, X. Sun, Photonic bandgap properties of two dimensional photonic quasicrystals with multiple complex structures, *Superlattice. Microst.* 129 (2019) 247–251, <https://doi.org/10.1016/j.spmi.2019.04.010>.
- [15] K. McLaughlin, D. Rabson, P. Thiel, Comment on “Origin of friction anisotropy on a quasicrystal surface” reply, *Phys. Rev. Lett.* 107 (2011), 209401. <https://doi.org/10.1103/PhysRevLett.104.074302>.
- [16] K. Lee, W. Dai, D. Naugle, H. Liang, Effects of microstructure of quasicrystal alloys on their mechanical and tribological performance, *J. Tribol.* 140 (2018) <https://doi.org/10.1115/1.4039528>.
- [17] K. Lee, J. Hsu, D. Naugle, H. Liang, Multi-phase quasicrystalline alloys for superior wear resistance, *Mater. Des.* 108 (2016) 440–447, <https://doi.org/10.1016/j.matdes.2016.06.113>.
- [18] B.N. Mordyuk, G.I. Prokopenko, Y.V. Milman, M.O. Iefimov, K.E. Grinkevych, A.V. Sameljuk, I.V. Tkachenko, Wear assessment of composite surface layers in Al-6Mg alloy reinforced with AlCuFe quasicrystalline particles: effects of particles size, microstructure and hardness, *Wear* 319 (2014) 84–95, <https://doi.org/10.1016/j.wear.2014.07.011>.
- [19] B.N. Mordyuk, Y.V. Milman, M.O. Iefimov, K.E. Grinkevych, Wear and friction behaviors of aluminum matrix composite layers mechanically reinforced with quasicrystalline or crystalline SiC particles, *J. Manuf. Technol. Res.* 9 (2017) 121–140 [https://www.researchgate.net/profile/Bohdan\\_Mordyuk/publication/324782743\\_Wear\\_and\\_friction\\_behaviours\\_of\\_aluminium\\_matrix\\_composite\\_layers\\_mechanically\\_reinforced\\_with\\_quasicrystalline\\_or\\_crystalline\\_SiC\\_particles/links/5ae205f2aca272fdaf8fa084/Wear-and-friction-behaviours-of-aluminium-matrix-composite-layers-mechanically-reinforced-with-quasicrystalline-or-crystalline-SiC-particles.pdf](https://www.researchgate.net/profile/Bohdan_Mordyuk/publication/324782743_Wear_and_friction_behaviours_of_aluminium_matrix_composite_layers_mechanically_reinforced_with_quasicrystalline_or_crystalline_SiC_particles/links/5ae205f2aca272fdaf8fa084/Wear-and-friction-behaviours-of-aluminium-matrix-composite-layers-mechanically-reinforced-with-quasicrystalline-or-crystalline-SiC-particles.pdf).
- [20] R.T. Li, Z.L. Dong, K.A. Khor, Al-Cr-Fe quasicrystals as novel reinforcements in Ti based composites consolidated using high pressure spark plasma sintering, *Mater. Des.* 102 (2016) 255–263, <https://doi.org/10.1016/j.matdes.2016.04.040>.
- [21] T.M.K. Tabonah, M. Akkas, S. Islak, Microstructure, wear and corrosion properties of NiB-TiC composite materials produced by powder metallurgy method, *Sci. Sinter.* 51 (2019) 1–13, <https://doi.org/10.2298/SOS1903327A>.
- [22] A. Jamwal, P. Prakash, D. Kumar, N. Singh, K.K. Sadasivuni, K. Harshit, S. Gupta, P. Gupta, Microstructure, wear and corrosion characteristics of Cu matrix reinforced SiC-graphite hybrid composites, *J. Compos. Mater.* 53 (2019) 2545–2553, <https://doi.org/10.1177/0021998319832961>.
- [23] A. Chen, S. Ding, J. Huang, J. Zhang, Y. Dong, X. Fu, B. Shi, B. Wang, Z. Zhang, Fabrication of superrepellent microstructured polypropylene/graphene surfaces with enhanced wear resistance, *J. Mater. Sci.* 54 (2019) 3914–3926, <https://doi.org/10.1007/s10853-018-3138-y>.
- [24] E. Katinas, M. Antonov, V. Jankauskas, R. Skirkus, Effect of WC grain size and content on erosive wear of manual arc welded hard facings with low-carbon ferritic-pearlitic steel or stainless steel matrix, *Key Eng. Mater.* 674 (2016) 213–218, <https://doi.org/10.4028/www.scientific.net/KEM.674.213>.
- [25] B.-C. Irene, Á.-F. Jesús, D.-F. Alejandro, Effect of grain size and density of abrasive on surface roughness, material removal rate and acoustic emission signal in rough honing processes, *Metals* (2019) 860, <https://doi.org/10.3390/met9080860>.
- [26] V.E. Ovcharenko, E.N. Boyangin, Effect of TiN nanoparticles on the grain size, wear resistance, and strength of the intermetallic compound  $Ni_3Al$ , *Inorg. Mater.* 52 (7) (2016) 729–734, <https://doi.org/10.1134/S0020168516070128>.
- [27] A. Jain, B. Basu, B.V. Manoj Kumar, Harshvardhan, J. Sarkar, Grain size-wear rate relationship for titanium in liquid nitrogen environment, *Acta Mater.* 58 (2010) 2313–2323, <https://doi.org/10.1016/j.actamat.2009.12.017>.
- [28] Z.-G. Wang, J.-H. Ouyang, Y.-H. Ma, Y.-J. Wang, L.-Y. Xie, Z.-G. Liu, A. Henniche, Y. Wang, Grain size dependence, mechanical properties and surface nanoeutectic modification of  $Al_2O_3$ - $ZrO_2$  ceramic, *Ceram. Int.* 45 (2019) 14297–14304, <https://doi.org/10.1016/j.ceramint.2019.04.140>.
- [29] H. Saito, A. Iwabuchi, T. Shimizu, Effects of Co content and WC grain size on wear of WC cemented carbide, *Wear* 261 (2006) 126–132, <https://doi.org/10.1016/j.wear.2005.09.034>.

- [31] J. Dai, H. Su, H. Hu, T. Yu, W. Zhou, W. Ding, S. Ji, Y. Zheng, The influence of grain geometry and wear conditions on the material removal mechanism in silicon carbide grinding with single grain, *Ceram. Int.* 43 (2017) 11973–11980, <https://doi.org/10.1016/j.ceramint.2017.06.047>.
- [32] Y. He, L. Winnubst, A.J. Burggraaf, H. Verweij, P.G.T. van der Varst, B. de With, Grain-size dependence of sliding wear in tetragonal zirconia polycrystals, *J. Am. Ceram. Soc.* 79 (1996) 3090–3096, <https://doi.org/10.1111/j.1151-2916.1996.tb08081.x>.
- [33] S.J. Bull, Failure modes in scratch adhesion testing, *Surf. Coat. Technol.* 50 (1991) 25–32, [https://doi.org/10.1016/0257-8972\(91\)90188-3](https://doi.org/10.1016/0257-8972(91)90188-3).
- [34] S.J. Bull, An overview of the potential of quantitative coating adhesion measurement by scratch testing, *Tribol. Int.* 39 (2006) 99–114, <https://doi.org/10.1016/j.triboint.2005.04.013>.
- [35] D.J. Sordelet, M.G. Besser, J.L. Logsdon, Abrasive wear behavior of Al-Cu-Fe quasi-crystalline composite coatings, *Mater. Sci. Eng. A* 225 (1998) 54–65, [https://doi.org/10.1016/S0921-5093\(98\)00778-3](https://doi.org/10.1016/S0921-5093(98)00778-3).
- [36] L. Tang, C. Gao, J. Huang, G. Zhang, W. Chang, Dry sliding friction and wear behavior of hardened AISI D2 tool steel with different hardness levels, *Tribol. Int.* 66 (2013) 165–173, <https://doi.org/10.1016/j.triboint.2013.05.006>.